Spectra and energy levels of $Tm^{3+}(4f^{12})$ in AlN

John B. Gruber
Department of Physics, San José State University, San José, California 95192-0106, USA

Ulrich Vetter and Hans Hofsäss
2. Physikalisches Institut, Universität Göttingen, Tammannstrasse 1, 37077 Göttingen, Germany

Bahram Zandi
ARL/Adelphi Laboratory Center, US Army, Adelphi, Maryland 20783-1197, USA

Michael F. Reid
Department of Physics and Astronomy, University of Canterbury, Christchurch, New Zealand
(Received 4 May 2004; revised manuscript received 31 August 2004; published 8 December 2004)

We report a detailed analysis of the cathodoluminescence spectra of Tm^{3+}-implanted 2H-aluminum nitride (AlN) covering the wavelength range between 290 and 820 nm at temperatures between 12 and 60 K. More than 200 transitions are observed, of which more than 100 of these transitions can be identified from emitting multiplet manifolds $^1I_6$, $^1D_2$, and $^1G_4$. Although the emitting levels are not observed directly, emission is also attributed to the $^3P_2$ and $^3P_1$ multiplet manifolds based on analyses of transitions to terminal levels $^3F_4$, $^3H_5$, and $^3F_3$. The observed crystal-field splitting of the ground-state multiplet manifold, $^3H_6$, and manifolds $^3F_4$, $^3H_5$, $^3H_4$, $^3F_3$, $^3F_2$, and $^1G_4$ is established from an analysis based on matching repeated energy differences between transitions. This method is similar to one used in analyzing arc and spark spectra. Temperature-dependent spectra also establish the crystal-field splitting of the $^3P_1$ and part of the manifold splitting of emitting levels such as $^1I_6$. To establish an initial set of crystal-field splitting parameters, B_{nm}, that can be related to a physical model, we carried out a lattice-sum calculation by computing the crystal-field components, which are the coefficients in a multipolar expansion of the crystal field about the Al^{3+} sites that have C_{3v} symmetry in the lattice. Emission channeling experiments indicate that the Al^{3+} sites serve as the substitutional sites for Tm^{3+} in AlN. With only minor adjustments to the calculated centroids to account for J-mixing, the calculated crystal-field splitting of most multiplet manifolds, $^{2S+1}L_J$, of $Tm^{3+}(4f^{12})$ based on the B_{nm} obtained from the lattice-sum calculations, is in good agreement with the reported experimental splitting.

DOI: 10.1103/PhysRevB.70.245108 PACS number(s): 78.40.Fy, 78.60.Hk, 71.70.Ch

I. INTRODUCTION

The radiative intra-$4f$ electron transitions of tripositive rare earth ions (RE^{3+}) doped into very wide band-gap semiconductors, such as 2H-aluminum nitride (AlN), are of considerable interest currently as these materials have promise for optoelectronic applications.[1–12] As a host semiconductor, AlN has a band gap of 6.2 eV; it has high thermal conductivity and is chemically inert in most environments.[8] Such a wide band gap exploits the ultraviolet energy levels of many RE^{3+} ions hidden to prominent hosts such as Si or GaN, the latter being the current host of choice for RE^{3+} ion light emitters.[13–19] The possibility of observing ultraviolet emission from $4f^n$ and $4f^{n-1}$ d states of RE^{3+} ions not only opens up fundamental spectroscopic studies,[12,20] but also makes these systems interesting candidates for phosphor illuminators playing an important role in the design of white light emitters.[21,22]

The potential of AlN as a host for RE^{3+} ions has been demonstrated by a number of groups for Er^{3+}- (Refs. 1–7), Eu^{3+} and Tb^{3+}- (Ref. 23), Tm^{3+}- (Refs. 24 and 25), and Gd^{3+}- (Ref. 12) doped AlN. However, limited implantation fluence can hinder the spectroscopic investigations necessary to identify the detailed crystal-field splitting of the energy levels of the rare earth ions. Ion implantation is not always the method used for doping. But in contrast to doping during growth, the use of ion implantation ensures that no additional impurities are incorporated (especially oxygen). Of particular concern has been the identification of the ion sites in the lattice. An attractive direct determination of the ion's lattice location is provided by the emission channeling (EC) technique which uses charged particles emitted in the decay of radioactive ions for location assignments.[24–28] This method benefits from the fact that nearly all rare earths provide a useable decay chain. In the present study, the lattice location of Tm^{3+} in AlN was determined using $^{169}Yb^{3+}$ ions implanted into the host.[24] EC studies have also been successful in determining the lattice locations of other rare earth ions in other semiconducting hosts.[26–28] In fact, the emission channeling studies of Pr in GaN (Ref. 26) allowed for a detailed crystal-field splitting analysis of the cathodoluminescence (CL) spectra of that material,[19,29] followed by similar analyses of Sm^{3+} and Tb^{3+} in GaN.[30,31] A remarkable outcome from those studies was the change in site symmetry of the RE^{3+} ions over the series which was attributed to a diminution of the ionic radii with increasing number of $4f$ electrons due to the lanthanide contraction.

In the present study, we report a detailed analysis of the cathodoluminescence (CL) spectra of Tm-implanted 2H-aluminum nitride covering the wavelength range between

290 and 820 nm, at temperatures between 12 and 60 K. More than 200 emission peaks and bands are observed, of which more than 100 represent transitions from emitting multiplet manifolds $^1I_6$, $^1D_2$ and $^1G_4$. Possible emission from the $^3P_2$ and $^3P_1$ is also reported to manifolds $^3F_4$, $^3H_5$, and $^3F_3$, but these results lack the direct observation of the emitting energy (Stark) levels for a confirmation. The observed crystal-field splitting of the ground-state multiplet manifold, $^3H_6$, and manifolds $^3F_4$, $^3H_5$, $^3H_4$, $^3F_3$, $^3F_2$, and $^1G_4$ are established from an analysis of the CL spectrum obtained at 12 K. Spectra observed at 30 and 60 K are instrumental in identifying part of the manifold splittings of the $^3P_1$, $^1I_6$, and $^1D_2$ levels from temperature-dependent transitions.

To model the detailed crystal-field splitting of individual multiplet manifolds, we began with the free-ion wave functions for $Tm^{3+}(4f^{12})$, starting with the Coulombic, spin-orbit, and interconfigurational interaction parameters reported by Carnall *et al.*[32] and Gruber *et al.*[33] To establish an initial set of crystal-field splitting parameters, B_{nm}, that can be related to a physical model, we performed a lattice-sum calculation by computing the crystal-field components, which are the coefficients in a multipolar expansion of the crystal field about the Al^{3+} sites that have C_{3v} symmetry in the lattice. These sites are identified by Vetter *et al.*[24] as the substitutional sites for Tm^{3+} based on emission channeling experiments.

With only a modest adjustment to the theoretical multiplet-manifold centroids based on the free-ion parameters given by Gruber *et al.*[33] and with no adjustment to the lattice-sum derived B_{nm} parameters, good agreement is obtained between the calculated and the experimental splitting of multiplet manifolds $^3H_5$, $^3F_3$, $^3F_2$, and $^1G_4$, including the splitting of $^3P_1$, inferred from the temperature-dependent transitions to the $^3H_5$ and $^3F_3$ multiplet manifolds. A least-squares fitting of both the centroids and the crystal-field splitting parameters improves agreement between the calculated and the experimental splitting of all observed multiplet manifolds, including the ground state manifold, $^3H_6$, and the $^3F_4$ and $^3H_4$ manifolds. The rms deviation between 37 calculated and observed Stark levels is 10 cm^{-1}. Bandwidth and structure associated with analyzed transitions precludes further inquiry as to the meaning of the overall rms deviation.

II. EXPERIMENTAL DETAILS AND OBSERVED SPECTRA

Films of AlN, grown on substrates of 6H-SiC (0001) by metal-organic chemical vapor deposition (MOCVD), were obtained from commercial sources. Upon receipt, the substrate was cut into small pieces, rinsed in acetone and deionized water, and dried under a flow of nitrogen gas. During implantation (fluence: 1×10^{13} ions/cm^2), samples were tilted 10° to the incident beam to avoid channeling by the incident ions. Postimplantation annealing was carried out in a vacuum tube furnace at pressures near 10^6 mbar and at a temperature of about 1373 K for 30 min.

For CL fluorescence measurements, implanted samples were mounted on the head of a closed-cycle helium refrigerator located inside the vacuum chamber. An electrically controlled resistive heater placed at the refrigerator head allows one to adjust the sample temperatures between 12 and 300 K. The excitation source consisted of a SPECS EQ22 Auger electron gun that provides electrons with energies in the range between 100 eV and 5 keV and beam currents between 0.01 and 150 μA.

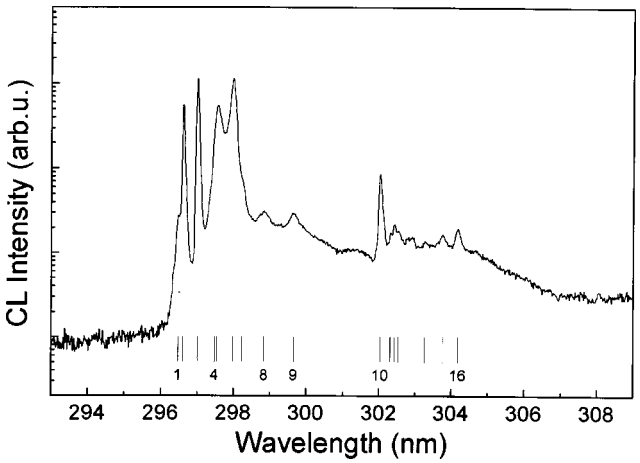

FIG. 1. The CL spectrum of $^1I_6 \rightarrow {}^3H_6$ (1–9) and $^3P_2 \rightarrow {}^3F_4$ (10–16) electronic transitions and phonon sidebands of Tm^{3+} in AlN, recorded at 30 K between 292 and 310 nm.

Sample luminescence was passed through a quartz window and collected with a UV-coated achromate lens pair before reaching the entrance slit of a Czerny-Turner spectrograph, model Jobin-Yvon 1000M. The light was dispersed using several holographic gratings, blazed at 300 and 700 nm, and with 1200 or 600 lines/mm, and detected by a nitrogen-cooled charge coupled device (CCD) camera, model Jobin-Yvon, UV-enhanced CCD (EEV CCD30-11). Exposure times for the spectra ranged from 5 to 10 s. The spectrograph was repeatedly calibrated using the air wavelengths of spectral lines from a mercury lamp standard. The uncertainty in wavelength measurements was about 0.05 nm maximally. The spectra are not corrected for the response function of the setup. Temperature-dependent measurements were made on transitions at a given wavelength without moving the grating or otherwise disturbing the experimental setup in order to minimize inaccuracies in the measurements.

Intrinsic broadband luminescence attributed to defects is observed in the visible and ultraviolet regions of the CL spectra of undoped AlN. The high resolution sharp-line fluorescence due to implanted Tm^{3+} in AlN is usually easy to recognize superimposed on the broadband luminescence since relatively small ranges of wavelengths are involved representing the observed transitions between the $Tm^{3+}(4f^{12})$ $^{2S+1}L_J$ manifolds. Examples of these transitions are shown in Figs. 1–5. Comparative spectroscopic analyses between undoped and doped samples are also useful to sort out the presence of impurities such as chromium and other rare earths. Following these diagnostic tests, we have established the identity of the Tm^{3+} spectra that are given in Tables I and II.

Analysis of the unpolarized Tm^{3+} CL spectra attributed to transitions between Stark levels is based on matching repeated energy differences between states similar to the method used in analyzing the arc and spark spectra of ions

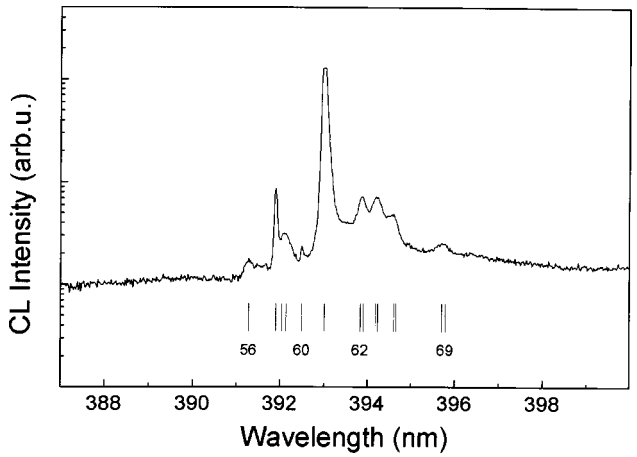

FIG. 2. The CL spectrum of $^1I_6 \rightarrow {}^3H_5$ (56–70) electronic transitions and phonon sidebands of Tm^{3+} in AlN, recorded at 12 K between 387 and 400 nm.

and gaseous molecules for their energy-level configurations. However, we are also aided by past analyses of the crystal-field splitting of Tm^{3+} energy levels in a variety of hosts. For example, in LaF_3 (Ref. 34) the two lowest-energy emitting Stark levels from $^1I_6$ are identified at 34 675 and 34 696 cm^{-1}; in $Y_3Al_5O_{12}$ (Ref. 33) these levels are found at 34 391 and 34 422 cm^{-1}; and in Y_2O_3 (Ref. 35) these levels are reported at 33 877 and 33 884 cm^{-1}. In the present study, an analysis of the CL spectra representing emission from $^1I_6$ to multiplet manifolds $^3H_6$, $^3F_4$, $^3H_5$, $^3H_4$, $^3F_3$, $^3F_2$, and $^1G_4$ shown in Table I place the emitting Stark levels of $^1I_6$ at 33 706 and 33 722 cm^{-1}.

In Fig. 1 transitions 1–9 represent the $^1I_6 \rightarrow {}^3H_6$ emission observed at 30 K. This spectrum observed at 60 K shows that transition 1 in Fig. 1 is temperature-dependent and represents a transition from the 33 722 cm^{-1} Stark level to the ground-state Stark level. Transition 2 represents a transition from the 33 706 cm^{-1} Stark level to the ground-state Stark level as well. The temperature-dependent spectra for $^1I_6$

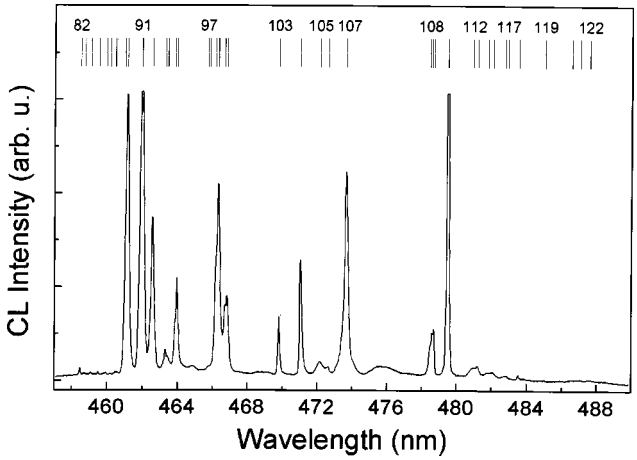

FIG. 3. The CL spectrum of $^1D_2 \rightarrow {}^3F_4$ (90–102), $^1I_6 \rightarrow {}^3H_4$ (103–111), and $^1G_4 \rightarrow {}^3H_6$ (108–122) electronic transitions and phonon sidebands of Tm^{3+} in AlN, recorded at 12 K between 460 and 488 nm.

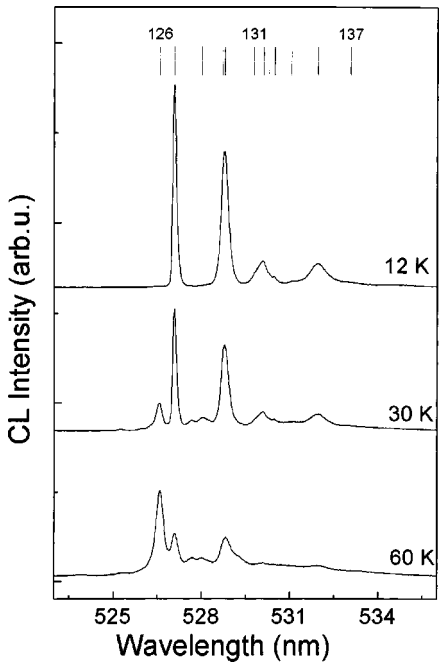

FIG. 4. The CL spectrum of $^1I_6 \rightarrow {}^3F_3$ (127–136), recorded at 12, 30, and 60 K and observed between 525 and 534 nm. Temperature-dependent transitions are observed at temperatures higher than 12 K.

$\rightarrow {}^3H_6$ not only provide information on part of the splitting of the $^1I_6$ multiplet, but a similar pattern of emission observed from the 33 722 cm^{-1} level also supports the splitting determined for $^3H_6$ analyzed on the basis of emission from the 33 706 cm^{-1} level. Furthermore, the splitting of $^3H_6$ has been confirmed by matching similar energy differences based on an analysis of the emission spectra observed from the $^1D_2$ and $^1G_4$ manifolds as shown in Tables I and II.

In Fig. 1 transitions 10–16 provide a splitting similar to the splitting of the $^3F_4$ manifold obtained from analyzing the CL spectra $^1I_6 \rightarrow {}^3F_4$, $^1D_2 \rightarrow {}^3F_4$, and $^1G_4 \rightarrow {}^3F_4$ (see Tables I and II). If we assume that transition 10 comes from an emitting Stark level in the $^3P_2$ manifold at 38 591 cm^{-1}, transi-

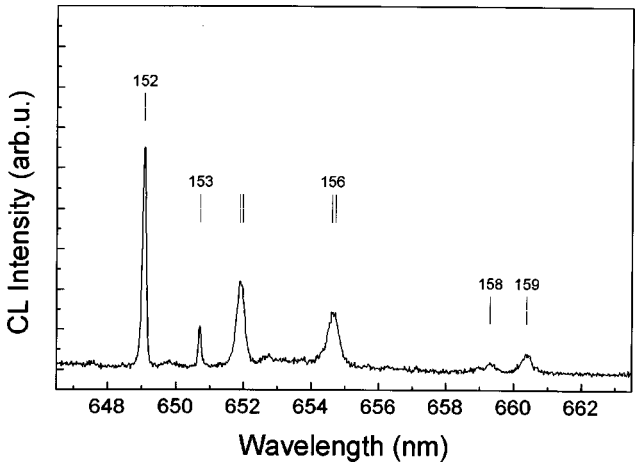

FIG. 5. The CL spectrum of $^1G_4 \rightarrow {}^3F_4$ (152–159) recorded at 12 K and observed between 648 and 662 nm.

TABLE I. Emission spectra from $^1I_6$ and $^1D_2$ to ^3H_J, ^3F_J, and $^1G_4$ observed at 12 K.

$\Delta(^{2S+1}L_J)$[a]	λ(nm)[b]	E(cm^{-1})[c] observed	Transition[d]	ΔE(cm^{-1})[e] observed	$\Delta(^{2S+1}L_J)$[a]	λ(nm)[b]	E(cm^{-1})[c] observed	Transition[d]	ΔE(cm^{-1})[e] observed
$^1I_6\rightarrow{}^3H_6$	296.46*	33 722	1		$^1D_2\rightarrow{}^3H_6$	368(sh)*	27 178	51(a)	
(33 706)	296.6	33 706	2	0	(27170)	368.06	27 170	51	0
	297.0	33 660	3	46		368.7	27 125	52	45
	297.47*	33 607	4						
	297.53	33 600	5	106		369.0	27 064	52(a)	106
	297.97	33 550	6	156		370.07	27 014	53	156
	298.23	33 521	7	185		370.4	26 985	54	185
	298.83*f*	33 454	8	252		371.4	26 918	55	252
	299.65*f*	33 363	9	343					
$^1I_6\rightarrow{}^3F_4$	354.32	28 215	19	5491	$^1D_2\rightarrow{}^3F_4$	461.15	21 679	90	5491
(33 706)	354.81	28 176	20	5530	(27 170)	461.97	21 640	91	5530
	355.16	28 148	21	5558		462.57	21 612	92	5558
	356.0	28 082	24	5624		463.95	21 547	96	5623
	357.37	27 974	28	5732		466.31	21 439	100	5731
	357.63	27 954	29	5752		466.82	21 417	102	5753
$^1I_6\rightarrow{}^3H_5$	391.9	25 509	57	8197	$^1D_2\rightarrow{}^3H_5$	526.9	18 974	126	8196
(33 706)	392.5	25 470	60	8236	(27 170)	528.01	18 934	128	8236
	393.01	25 437	61	8269		528.79	18 904	130	8266
	394.18	25 362	64	8344		531.05	18 827	135	8343
	394.6	25 342	66	8364		532.0(sh)	18 804	135(sh)	8366
	396.(b)	25 240	69	8466		534.6(b)	18 704	137	8466
$^1I_6\rightarrow{}^3H_4$	469.79	21 280	103	12 426	$^1D_2\rightarrow{}^3H_4$	678.08	14 743	161	12 427
(33 706)	471.01	21 225	104	12 481	(27 170)	680.59	14 691	163	12 479
	472.14	21 174	105	12 532		682.04	14 658	165	12 512
	472.62*	21 153	106			684.01*	14 616	168	
	473.65	21 107	107	12 599		686.14	14 570	171	12 600
	470.0(b)	21 008	107(a)	12 698		491(b,w)	14 472	172	12 698
$^1I_6\rightarrow{}^3F_3$	527.08	18 967	127	14 739	$^1D_2\rightarrow{}^3F_3$	804.5	12 430	191	14 740
(33 706)	528.72	18 908	129	14 798	(27 170)	808.7	12 368	197	14 802
	530.11	18 859	132	14 847		811.3	12 323	199	14 847
	530.48	18 846	134	14 860		812.08	12 311	200	14 859
	531.96	18 793	136	14 913		813.57	12 288	201	14 882
$^1I_6\rightarrow{}^3F_2$	544.4	18 364	139	15 342					
(33 706)	546.21	18 303	142	15 403					
	548.49	18 226	144	15 480					
$^1I_6\rightarrow{}^1G_4$	780.37	12 812	184	20 894					
(33 706)	780.44	12 809	185	20 897					
	798.0(b)	12 530	191	21 176					
	804.66	12 425	192	21 281					
	807.63	12 379	196	21 327					
	811.3(b)	12 323	199	21 383					

[a]Multiplet manifold transitions; emitting Stark level in parentheses.
[b]Wavelength in nanometers; sh denotes shoulder; b denotes broad; * denotes temperature dependent.
[c]Energy of transition in vacuum wave numbers.
[d]Transitions label (Stark level to Stark level) as shown in figures 1–5.
[e]Energy difference (cm^{-1}) with emitting level in parentheses in Columns 1 and 6.
[f]Broadband with structure.

TABLE II. Emission spectra from $^1G_4$ and $^3P_1$ to $^3H_6$, $^3F_4$, $^3H_5$, and $^3F_3$ observed at 12 K.

$\Delta(^{2S+1}L_J)$[a]	λ(nm)[b]	$E(cm^{-1})$[c] observed	Transition[d]	$\Delta E(cm^{-1})$[e] observed	$\Delta(^{2S+1}L_J)$[a]	λ(nm)[b]	$E(cm^{-1})$[c] observed	Transition[d]	$\Delta E(cm^{-1})$[e] observed
$^1G_4 \rightarrow {}^3H_6$	478.46	20 894	108[f]	0	$^3P_1 \rightarrow {}^3H_5$	355.59	28 114	22	8197
(20 894)	478.59	20 889	109[f]		(36 311)	356	28 075	25	8236
	479.5	20 849	111	45		356.49	28 043	26	8268
	480.95	20 786	112	108		357.4	27 968	28	8343
	481.2	20 776	113			357.72	27 947	30	8364
	481.78	20 751	114						
	482.07	20 738	115	156		359.03	27 845	32	8466
	482.78	20 708	116	186					
	482.79	20 702	117						
	483.52	20 676	118						
	485.01	20 612	119						
$^1G_4 \rightarrow {}^3F_4$	649.07	15 403	152	5491	$^3P_1 \rightarrow {}^3F_3$	463.44	21 572	94	14 739
(20 894)	650.71	15 364	153	5530	(36 311)	465	21 510	97	14 801
	651.89	15 336	154	5558		465.82	21 462	98	14 849
	654.62	15 271	156	5623		466.16	21 447	99	14 864
	659.31	15 163	158	5731		466.69	21 422	101	14 889
	660.38	16 140	159	5754					

[a]Multiplet manifold transitions; emitting Stark level in parentheses.
[b]Wavelength in nanometers; sh denotes shoulder; b denotes broad.
[c]Energy of transition in vacuum wave numbers.
[d]Transitions label (Stark level to Stark level) as shown in figures.
[e]Energy difference (cm^{-1}) with emitting level in parentheses in Columns 1 and 6.
[f]Transitions 108–110 (Fig. 3) represent a peak with structure; the shape does not appear to change at higher temepratures; it is possible that more than a single emitting level may be involved within a range of 6 cm^{-1}; in this case we choose a pattern that gives a similar splitting for the $^3H_6$ as observed from $^1I_6$ and $^1D_2$; the calculated splitting for the two lowest-energy Stark levels in $^1G_4$ are 20 895 and 20 908 cm^{-1} (Table IV, column 3).

tions labeled 10, 12, 13, 14, 16, and 16*a* give a splitting of $^3F_4$ as 5491, 5532, 5552, 5626, 5729, and 5754, respectively, in units of cm^{-1}. The emitting level, 38 591 cm^{-1}, can be compared with the lowest-energy Stark level in $^3P_2$ in other host crystals such as LaF_3 (Ref. 34) (38 250 cm^{-1}), $Y_3Al_5O_{12}$ (Ref. 33) (38 098 cm^{-1}), and Y_2O_3 (Ref. 35) (38 157 cm^{-1}). Excitation of the $^3P_2$ and $^3P_1$ levels is possible although the excitation mechanisms are not well understood. One mechanism of interest proposed by Lozykowski[36] suggests that the RE^{3+} ions create isoelectronic traps which may act as carrier traps. Once a carrier is trapped the complex is charged and may attract a carrier of opposite charge. This leads to the formation of a bound exciton, which excites the 4-*f* system. This excitation mechanism has a much larger cross section compared to impact excitation or ionization, and is believed to be the dominant excitation mechanism in our case. A detailed knowledge of the excitation of the Tm^{3+} levels in AlN is not given in our case. The population of individual manifolds may be due to direct excitation, energy transfer involving cross relaxation, down-conversion, and other mechanisms, and are affected by many other parameters such as the relative energetic position of these manifolds with respect to the conduction and valence band of the host.

In Table II we list the CL spectra for $^3P_1 \rightarrow {}^3H_5$ and $^3P_1 \rightarrow {}^3F_3$. The splitting of the $^3H_5$ and $^3F_3$ manifolds have been confirmed by emission from $^1I_6$ and $^1D_2$ to these manifolds (Table I). The emitting level from $^3P_1$ (36 311 cm^{-1}) can be compared with the emitting $^3P_1$ level in LaF_3 (Ref. 34) (36 531 cm^{-1}); $Y_3Al_5O_{12}$ (Ref. 33) (36 234 cm^{-1}), and Y_2O_3 (Ref. 35) (36 325 cm^{-1}). CL spectra obtained at 60 K also indicate temperature-dependent transitions that place the upper Stark level of $^3P_1$ at 36 360 cm^{-1} in agreement with the calculated Stark level reported later in this study. It is interesting to note that the transitions from 36 531 cm^{-1} to $^3H_5$, namely 22, 25, 26, 28, 30, and 32, overlap the $^1I_6 \rightarrow {}^3F_4$ transitions in Table I and the transitions from 36 531 cm^{-1} to $^3F_3$, namely 94, 97, 98, 99, and 101, overlap the $^1D_2 \rightarrow {}^3F_4$ transitions in Table I, making individual Stark level assignments within the four multiplet manifolds a challenge overcome by assignments made to these manifolds from other data reported in Tables I and II.

Figure 2 represents the 12 K CL spectrum for $^1I_6 \rightarrow {}^3H_5$. The observed transitions 57, 60, 61, 64, 66, and 69 provide a splitting pattern similar to one observed for $^1D_2 \rightarrow {}^3H_5$ spectra (Table I). The temperature-dependent transition 56 also forms a similar splitting pattern for temperature-dependent transitions observed in the 60 K spectrum.

Figure 3 shows the 12 K CL spectrum for $^1D_2 \rightarrow {}^3F_4$, transitions 90–102, Table I. Temperature-dependent transitions such as 89, 93, 95, and 101 help establish the splitting between the two emitting Stark levels of $^1D_2$, which are sepa-

rated by about 8 cm^{-1}. The calculated splitting for $^1D_2$ based on the modeling reported in the next section predicts Stark levels at 27 170, 27 191, and 27 240 cm^{-1}. The observed splitting of 27 170 cm^{-1} (Table I) and 27 178 cm^{-1} are in reasonable agreement with the calculated values. At higher temperatures there is evidence for the third Stark level appearing at 27 235 cm^{-1}. Figure 3 also shows the 12 K CL spectra for $^1I_6 \rightarrow {}^3H_4$ beginning with transition 103 and overlapping the $^1G_4 \rightarrow {}^3H_6$ transitions that start with transitions 108–122. Transitions 108–110 suggest structure, perhaps due to close-lying Stark levels in $^1G_4$. The CL spectrum $^1I_6 \rightarrow {}^1G_4$ (transitions 184–199, Table I) indicate two levels, 20 894 and 20 900 cm^{-1}, which are confirmed by the calculated splitting of 20 895 and 20 908 cm^{-1}.

In Fig. 4 we observe the splitting of $^3F_3$ based on transitions 127, 129, 132, 134 (shoulder), and 136 originating from the $^1I_6$ (33 706 cm^{-1} Stark level). Emission from $^1I_6$ (33 722 cm^{-1}) can be seen (transition 126) in comparing the 12, 30, and 60 K CL spectra in Fig. 4. Other temperature-dependent peaks establish the splitting of $^3F_3$ from this excited Stark level as well. In Fig. 5 we see clear splitting of the $^3F_4$ manifold in the 12 K CL spectrum of $^1G_4 \rightarrow {}^3F_4$ that includes transitions 152, 153, 154, 156, 158, and 159 (Table II).

III. MODELING THE CRYSTAL-FIELD SPLITTING

The free-ion wave functions were calculated by diagonalizing in a Russell-Saunders basis of LSJ states a Hamiltonian that includes the Coulombic interactions in the form of the Racah parameters $E^{(1)}$, $E^{(2)}$, and $E^{(3)}$, the spin-orbit parameter ζ, and the generalized Trees' interconfiguration interaction in the form of parameters α, β, and γ. From our earlier work involving Tm^{3+} in other host crystals,[33] we chose for the present calculation: $E^{(1)}=7142.4$, $E^{(2)}=33.795$, $E^{(3)}=674.27$, $\zeta=2628.7$, $\alpha=14.677$, $\beta=-631.79$, and $\gamma=0$, all in cm^{-1}. These parameters were used to calculate the reduced matrix elements of U_2, U_4, and U_6 between all the intermediate-coupled wave functions for the $4f^{12}$ electronic configuration.

A separate program[37] takes the reduced matrix elements between the free-ion multiplets, sets up the crystal spaces for a given crystal-field symmetry, and diagonalizes in that space of multiplets the crystal-field splitting Hamiltonian

$$H_{\mathrm{CF}} = \sum_{n,m} B^{+}_{\mathrm{nm}} \sum_{i} C_{\mathrm{nm}}(\hat{r}_i), \tag{1}$$

where the B_{nm} represent the crystal-field splitting parameters, and where the complex conjugate satisfies the relation

$$B^{+}_{\mathrm{nm}} = (-1)^m B_{n,-m}. \tag{2}$$

The expressions $C_{\mathrm{nm}}(\hat{r}_i)$ in Eq. (1) are related to the standard spherical harmonics through the expression

$$C_{\mathrm{nm}}(\hat{r}) = [4\pi/(2n+1)]^{1/2} Y_{n,m}. \tag{3}$$

In Eq. (1), i is summed over the twelve $4f$ electrons of Tm^{3+}; $n=2$, 4, and 6, and m is restricted to 0, ±3, and ±6 by symmetry considerations. In C_{3v} symmetry there are six parameters (all real), namely, B_{20}, B_{40}, B_{43}, B_{60}, B_{63}, and B_{66}. The wave function chosen for a basis for the calculation of the crystal field is given by Morrison and Leavitt.[38] The free-ion wave functions, using the parameters given earlier, were used to calculate the matrix elements of the crystal field of Eq. (1).

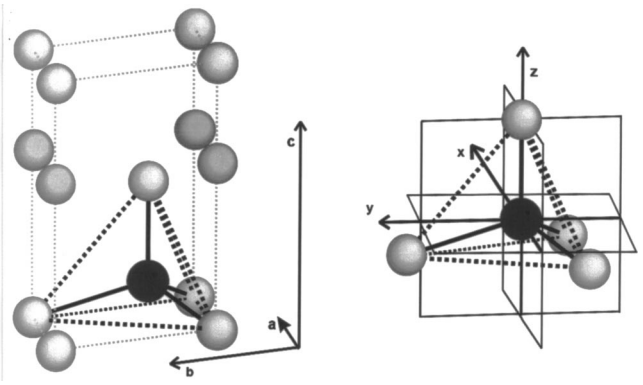

FIG. 6. The local symmetry and the coordination surrounding the Tm^{3+} ion (black) in Al^{3+} sites of C_{3v} symmetry in AlN.

The multiplet centroids obtained from diagonalizing the free-ion Hamiltonian can be varied in our program to obtain as close a fitting to the experimental centroids as possible, allowing for adjustments due to J mixing. The centroids thus obtained can be interpreted as the free-ion centroids that would be observed in the absence of the even components of the static crystal field. However, lacking a confirmation of the experimental ^3P_J centroids, we do not have sufficient data to establish an experimental set of free-ion parameters for Tm^{3+} in AlN and so we use the free-ion wave functions from Ref. 33.

To establish an initial set of B_{nm} that could be related to a physical model, we performed a lattice-sum calculation by computing the crystal-field components, A_{nm}, which are the coefficients in a multipolar expansion of the crystal field about the sites occupied by the Tm^{3+} ions in AlN. The total multipole field can be expressed in terms of lattice-sum components

$$A_{\mathrm{nm}} = -e^2 \sum_{j} q_j C_{\mathrm{nm}}(\hat{R}_j)/R_j^{n+1}, \tag{4}$$

where q_j is the effective electrostatic charge at the lattice site (R_j), and the sum is taken over all sites in the lattice. These calculations include point charges, dipoles, and quadrupoles in parameterized form.[37–40]

In Fig. 6 we show the local symmetry for Tm^{3+} in the w-AlN unit cell, as it replaces an Al^{3+} ion. The upper nitrogen ligand to the Tm^{3+} is separated by 1.50 Å while the lower three nitrogen ligands are equally separated by 1.80 Å. The axis of highest symmetry (C_3) is chosen as the z axis and corresponds to the c axis in the w-AlN unit cell. The hexagonal structure is characterized by the space group $C^4_{6v}-P6_3$ with cell parameters $a=b=3.11200$ Å, $c=4.99820$ Å, $\alpha=\beta=90°$, and $\gamma=120°$ (Refs. 41 and 42). These data are used to calculate the lattice-sum components in Eq. (4). Since the even-sum components are of primary importance

TABLE III. Lattice sums, A_{nm} (even n), and crystal-field parameters, B_{nm}.[a]

nm	A_{nm}	B_{nm}(I)[b]	B_{nm}(II)[c]
20	−1200	−207	−183
40	−1330	−538	−471
43	−2240	−908	−923
60	929	897	936
63	−510	−493	−472
66	558	538	554

[a]Lattice sums in units cm^{-1} $Å^{-n}$; B_{nm} in units of cm^{-1}; $\rho_2=0.1722$, $\rho_4=0.4053$, $\rho_6=0.9649$ in units of $Å^n$.
[b]Crystal-field parameters from lattice-sum calculations.
[c]Final set of B_{nm} obtained from least-squares fitting analysis.

for crystal-field splitting calculations, we list the values for A_{20}, A_{40}, A_{43}, A_{60}, A_{63} and A_{66} in Table III for Al^{3+} in C_{3v} symmetry sites in AlN.

The lattice-sum components given in Table III have been corrected for shielding and scaling factors that arise due to the expansion of the radial part of the free-ion wave function in the lattice host.[38–40] The accuracy of the lattice-sum parameters depends on the accuracy of the data obtained from the x-ray crystallography of the AlN samples. That is, the position of every ion in the unit cell must be established to the best possible value given the conditions of sample preparation. Those values ultimately dictate the number of significant figures for the A_{nm} listed in Table III. Based on a survey of available x-ray crystallographic data obtained from AlN samples similar to those used in this study,[37–42] the A_{nm} values calculated using Eq. (4) are quoted to three significant figures in Table III. These values have sufficient accuracy given the resolution of the spectral data.

The lattice-sum components A_{nm} are related to the crystal-field splitting parameters, B_{nm}, as follows:

$$B_{nm} = \rho_n A_{nm}, \tag{5}$$

where $\rho_2=0.1722$, $\rho_4=0.4033$, and $\rho_6=0.9649$ for Tm^{3+} $(4f^{12})$. We list the B_{nm} parameters for Tm^{3+} in Al^{3+} sites of C_{3v} symmetry in column 3 of Table III. These parameters based on the lattice-sum calculation are used to calculate the crystal-field splitting of the multiplet manifolds of Tm^{3+} $(4f^{12})$ in Table IV (column 3). The splittings are established relative to the calculated centroid splitting for that manifold (see Table IV, column 1), which was adjusted by a least-squares fitting method to account for J mixing. Our methods of calculation follow the approach we used earlier in analyzing the CL spectra of Pr^{3+}, Sm^{3+}, and Tb^{3+} in GaN.[29–31]

IV. DISCUSSION OF RESULTS

Without adjustment to the lattice-sum derived B_{nm}, the calculated splitting for $^3P_1$, $^3F_3$, $^3F_2$, $^1G_4$ and $^3H_5$ multiplet manifolds is in good agreement with the experimental splittings reported in Table IV. In Fig. 4, for example, peaks 127, 129, 132, 134, and 136 representing transitions from Stark level 33 706 cm^{-1} ($^1I_6$) establish Stark levels in the $^3F_3$ manifold as 14 739, 14 798, 14 847, 14 860, and 14 913 cm^{-1}, respectively. These levels are compared with a calculated splitting of 14 739, 14 801, 14 845, 14 859, and 14 878 cm^{-1}, respectively. The major peaks and the sharply defined shoulder (transition 134) observed in Fig. 4 are accounted for in the calculation given for $^3F_3$ in Table IV (column 3).

The $^3H_5$ splitting (Fig. 2) also provides a test of agreement between calculated and observed levels that together with the $^3F_3$ engages all six B_{nm} parameters, with a total of ten experimental splittings. Peaks 57, 60, 61, 64, 66, and 69, representing transitions from Stark level 33 706 cm^{-1} ($^1I_6$), establish Stark levels in the $^3H_5$ manifold, 8197, 8236, 8269, 8344, 8364, and 8466 cm^{-1}. A broadband observed at the shorter wavelength to peak 69 places a final expected Stark level at 8500 cm^{-1}. These levels can be compared with the calculated splitting based on the lattice-sum derived B_{nm} as follows: 8197, 8226, 8272, 8357, 8367, 8498, and 8508 cm^{-1}, respectively. Also, the experimental splitting of $^3P_1$ (36 311 and 36 360 cm^{-1}) can be compared favorably with a calculated splitting of 36 311 and 36 374 cm^{-1}, and the observed splitting of $^3F_2$, namely, 15 342, 15 403, and 15 480, all in cm^{-1}, are in reasonable agreement with calculated levels 15 342, 15 418, and 15 461, all in cm^{-1}. Again, no adjustment was made to the lattice-sum derived B_{nm} parameters used in calculating the splitting in column 3 of Table IV.

The splitting of the ground-state manifold $^3H_6$, and the splittings of the $^3H_4$ and $^3F_4$ manifolds are more problematic in their interpretation, due in part to emission from two relatively closely spaced Stark levels in emitting $^1I_6$ (transitions 1 and 2, Fig. 1) and $^1G_4$ (transitions 108 and 109, Fig. 3), and partly due to the relatively large crystal-field splitting matrix elements for these manifolds, which with small adjustments to the B_{nm}, produce considerable changes in the manifold splitting. In Fig. 1, if we take transition 2 as a transition to the ground-state Stark level from $^1I_6$ at 33 706 cm^{-1}, a partial splitting of the $^3H_6$ can be ascertained as 0 cm^{-1} (2), 46 cm^{-1} (3), 106 cm^{-1} (5), 156 cm^{-1} (6), 185 cm^{-1} (7), 252 cm^{-1} (8), and 343 cm^{-1} (9), with the numbers in parentheses representing the transitions given in Fig. 1 and Table I. This splitting can be compared with the calculated splitting of 0, 41, 128, 137, 218, 263, and 341 all in cm^{-1}. In Fig. 3, transitions from the $^1G_4$ to the $^3H_6$ manifold observed at 12 K are labeled 108–122. If we take the transition with structure at 478.46 nm (108) as representative of a transition from $^1G_4$ (20 894 cm^{-1}) to $^3H_6$, we obtain the following splitting for the $^3H_6$ manifold: 0 cm^{-1} (108), 45 cm^{-1} (111), 108 cm^{-1} (112), 156 cm^{-1} (115), and 186 cm^{-1} (116) where the number in parentheses represent the transition label in Fig. 3 and Table II. Other transitions observed in the $^1G_4$ spectrum are likely associated with the structure observed in transitions 108–110 that suggest more than a single emitting Stark level is involved. The calculated splitting for $^1G_4$ in Table IV, column 3, predicts emitting Stark levels at 20 895 and 20 908 cm^{-1}. Since, we have not observed all the Stark levels for the $^3H_6$ manifold, and indeed some of the broad band structure in Figs. 1 and 3 contain unresolved and

TABLE IV. Crystal-field splitting of $Tm^{3+}(4f^{12})$ energy levels in AlN.

$^{2S+1}L_J$[a]	$E(cm^{-1})$[b] experiment	$E(cm^{-1})$[c] calculated (I)	$E(cm^{-1})$[d] calculated (II)	Γ_n(calculated)[e]	Free-ion mixture of states[f]
$^3H_6$	0	0	0	$\Gamma_{1,2}$	$99.8\,^3H_6+0.15\,^3F_4+0.01\,^3H_4$
(277)	46	41	48	$\Gamma_{1,2}$	$99.9\,^3H_6+0.11\,^3F_4+0.01\,^3H_5$
	106	128	126	Γ_3	$99.9\,^3H_6+0.10\,^3F_4+0.03\,^3H_5$
	156	137	148	$\Gamma_{1,2}$	$99.8\,^3H_6+0.15\,^3F_4+0.02\,^3H_4$
	185	218	197	Γ_3	$99.9\,^3H_6+0.02\,^3H_5+0.01\,^3F_4$
	252	263	252	$\Gamma_{1,2}$	$99.9\,^3H_6+0.06\,^3F_4+0.01\,^3H_4$
	343	341	351	Γ_3	$99.9\,^3H_6+0.06\,^3H_5+0.02\,^3F_4$
		482	487	Γ_3	$99.9\,^3H_6+0.04\,^3H_5+0.04\,^3F_4$
		508	514	$\Gamma_{1,2}$	$99.9\,^3H_6+0.05\,^3F_4+0.03\,^3F_3$
$^3F_4$	5491	5491	5495	$\Gamma_{1,2}$	$99.7\,^3F_4+0.17\,^3H_5+0.07\,^3H_6$
(5689)	5530	5499	5512	Γ_3	$99.9\,^3F_4+0.05\,^3H_5+0.03\,^3H_4$
	5558	5689	5575	$\Gamma_{1,2}$	$99.5\,^3F_4+0.35\,^3H_5+0.18\,^3H_6$
	5624	5757	5644	$\Gamma_{1,2}$	$99.5\,^3F_4+0.27\,^3H_6+0.22\,^3H_5$
	5732	5763	5739	Γ_3	$99.0\,^3F_4+0.90\,^3H_5+0.04\,^3H_6$
	5752	5827	5773	Γ_3	$99.3\,^3F_4+0.59\,^3H_5+0.10\,^3H_6$
$^3H_5$	8197	8197	8195	Γ_3	$99.4\,^3H_5+0.40\,^3F_4+0.06\,^3H_4$
(8340)	8236	8226	8217	$\Gamma_{1,2}$	$99.5\,^3H_5+0.37\,^3F_4+0.06\,^3F_3$
	8269	8272	8265	Γ_3	$99.2\,^3H_5+0.48\,^3F_4+0.16\,^3H_4$
	8344	8357	8354	$\Gamma_{1,2}$	$99.8\,^3H_5+0.11\,^3F_4+0.06\,^3H_6$
	8364	8367	8359	Γ_3	$99.6\,^3H_5+0.32\,^3F_4+0.04\,^3H_6$
	8466	8498	8492	Γ_3	$99.3\,^3H_5+0.56\,^3F_4+0.06\,^3H_4$
	8500	8508	8500	$\Gamma_{1,2}$	$99.8\,^3H_5+0.09\,^3F_4+0.04\,^3F_4$
$^3H_4$	12 426	12 426	12 417	Γ_3	$99.4\,^3H_4+0.37\,^3F_3+0.09\,^3H_5$
(12 594)	12 481	12 501	12 491	$\Gamma_{1,2}$	$99.1\,^3H_4+0.57\,^3F_3+0.27\,^3F_2$
	12 532	12 507	12 522	Γ_3	$99.5\,^3H_4+0.17\,^2F_3+0.15\,^3H_5$
	12 599	12 659	12 620	Γ_3	$99.4\,^3H_4+0.44\,^3F_3+0.08\,^3H_5$
	12 698	12 719	12 705	$\Gamma_{1,2}$	$99.8\,^3H_4+0.11\,^3H_5+0.05\,^3F_3$
		12 879	12 865	$\Gamma_{1,2}$	$99.4\,^3H_4+0.54\,^3F_3+0.03\,^1G_4$
$^3F_3$	14 739	14 739	14 740	$\Gamma_{1,2}$	$99.7\,^3F_3+0.16\,^3H_4+0.08\,^3F_2$
(14 822)	14 798	14 801	14 802	Γ_3	$99.3\,^3F_3+0.30\,^3H_4+0.29\,^3F_2$
	14 847	14 845	14 844	$\Gamma_{1,2}$	$96.1\,^3F_3+3.13\,^3F_2+0.74\,^3H_4$
	14 860	14 859	14 858	$\Gamma_{1,2}$	$99.8\,^3F_3+0.09\,^3H_4+0.04\,^3H_5$
	14 913	14 878	14 882	Γ_3	$97.3\,^3F_3+2.00\,^3F_2+0.60\,^3H_4$
$^3F_2$	15 342	15 342	15 345	Γ_3	$99.6\,^3F_2+0.16\,^3H_5+0.15\,^3H_4$
(15 375)	15 403	15 418	15 418	Γ_1	$96.4\,^3F_2+3.02\,^3F_3+0.45\,^3H_4$
	15 480	15 461	15 462	Γ_3	$97.6\,^3F_2+2.13\,^3F_3+0.20\,^3H_4$
$^1G_4$	20 894	20 895	20 894	$\Gamma_{1,2}$	$99.9\,^1G_4+0.07\,^3F_3+0.04\,^1I_6$
(21 171)	20.897[g]	20 908	20 897	Γ_3	$99.8\,^1G_4+0.05\,^3F_3+0.04\,^1I_6$
	21 176	21 167	21 165	$\Gamma_{1,2}$	$99.9\,^1G_4+0.02\,^1I_6+0.01\,^3H_4$
	21 281	21 269	21 279	$\Gamma_{1,2}$	$99.9\,^1G_4+0.04\,^3F_3+0.03\,^1I_6$

TABLE IV. (*Continued.*)

$^{2S+1}L_J$[a]	$E(cm^{-1})$[b] experiment	$E(cm^{-1})$[c] calculated (I)	$E(cm^{-1})$[d] calculated (II)	Γ_n(calculated)[e]	Free-ion mixture of states[f]
	21 327	21 311	21 333	Γ_3	$99.9\ ^1G_4+0.04\ ^1I_6+0.03\ ^1D_2$
	21 383	21 387	21 387	Γ_3	$99.9\ ^1G_4+0.04\ ^1I_6+0.02\ ^3H_4$
$^1D_2$	27 170	27 170	27 170	Γ_1	$99.9\ ^1D_2+0.05\ ^1I_6+0.02\ ^1G_4$
(27 206)	27 178[g]	27 191	27 184	Γ_3	$99.8\ ^1D_2+0.12\ ^1I_6+0.03\ ^1G_4$
	27 230[g]	27 240	27 233	Γ_3	$99.8\ ^1D_2+0.11\ ^1I_6+0.03\ ^1G_4$
$^1I_6$	33 706	33 706	33 706	Γ_3	$99.9\ ^1I_6+0.06\ ^3P_2+0.04\ ^1D_2$
(33 965)	33 722[g]	33 767	33 730	Γ_3	$99.8\ ^1I_6+0.10\ ^3P_2+0.06\ ^1D_2$
	33 745[g]	33 789	33 751	$\Gamma_{1,2}$	$99.9\ ^1I_6+0.03\ ^1G_4+0.01\ ^3P_2$
	33 772[g]	33 859	33 781	$\Gamma_{1,2}$	$99.9\ ^1I_6+0.02\ ^3P_0+0.01\ ^1G_4$
		33 978	33 913	$\Gamma_{1,2}$	$99.9\ ^1I_6+0.01\ ^1G_4+0.01\ ^3P_0$
		34 070	34 038	$\Gamma_{1,2}$	$99.9\ ^1I_6+0.04\ ^3P_0+0.01\ ^1G_4$
		34 119	34 095	Γ_3	$99.7\ ^1I_6+0.17\ ^3P_2+0.11\ ^1D_2$
		34 221	34 181	Γ_3	$99.9\ ^1I_6+0.04\ ^3P_2+0.03\ ^1G_4$
		34 261	34 216	$\Gamma_{1,2}$	$99.5\ ^1I_6+0.31\ ^3P_0+0.10\ ^3P_2$
$^3P_0$		35 279		Γ_1	$99.6\ ^3P_0+0.38\ ^1I_6+0.01\ ^3P_2$
(35 312)					
$^3P_1$	36 311	36 311	36 311	Γ_3	$99.9\ ^3P_1+0.03\ ^3P_2+0.01\ ^3H_4$
(36 332)	36 360[g]	36 374	36 368	Γ_1	$99.9\ ^3P_1+0.01\ ^3H_4+0.01\ ^3F_3$
$^3P_2$	38 591	38 591	38 591	Γ_3	$99.8\ ^3P_2+0.14\ ^1I_6+0.02\ ^3P_1$
(38 710)		38 738	38 715	Γ_1	$99.9\ ^3P_2+0.01\ ^1I_6+0.02\ ^3P_0$
		38 845	38 840	Γ_3	$99.7\ ^3P_2+0.24\ ^1I_6+0.01\ ^1D_2$
$^1S_0$		79 598		Γ_1	$99.9\ ^1S_0+0.10\ ^1I_6$
(79 592)					

[a]Multiplet manifold; number in parentheses is the calculated centroid.
[b]Experimental energy (Stark) level in cm^{-1}; based on energy differences reported in Table I and II (columns 5 and 10).
[c]Calculated splitting using the crystal-field splitting parameters obtained from the lattice-sum calculation (Table III, column 3); only the calculated centroids are varied in order to account for J mixing.
[d]Centroids and B_{nm} are varied; the rms for 37 calculated to experimental Stark levels is 10 cm^{-1}; the set of B_{nm} are given in Table III, column 4.
[e]The crystal quantum number labels are given based on the lattice-sum calculation; $\Gamma_{1,2}$ is nondegenerate and is either Γ_1 or Γ_2, our program does not distinguish between the two; Γ_3 is twofold degenerate in C_{3v} symmetry; $Tm^{3+}(4f^{12})$ is a non-Kramers ion with a singlet ground state predicted for Tm^{3+} in AlN.
[f]Percent free-ion mixture of states based on lattice-sum B_{nm}.
[g]Identified from 60 K emission spectra; not used in least-squares fitting analysis.

temperature-dependent spectra that obscure further analysis, we are not able to complete Stark level assignments within the $^3H_6$ manifold. However, for what we have identified experimentally, the calculated splitting appears reasonable.

The splitting of the $^3H_4$ manifold given in Table I is based on emission from $^1I_6$ and $^1D_2$. In Fig. 3 we observe transitions from $^1I_6$ (33 706 cm^{-1}) to $^3H_4$ Stark levels 12 426 cm^{-1} (103), 12 481 cm^{-1} (104), 12 532 cm^{-1} (105), and 12 599 cm^{-1} (107). A band at 476 (b) nm, may be associated with a $^3H_4$ Stark level expected around 12 698 cm^{-1}. Additional structure representing the highest-energy Stark level predicted in the $^3H_4$ manifold (12 879 cm^{-1}) may be lost in

the structure of the emission from $^1G_4$ to $^3H_6$. The calculated splitting based on the lattice-sum derived B_{nm} (Table IV, column 3) is 12 426, 12 501, 12 507, 12 659, 12 719, and 12 879 cm^{-1}. The calculated splitting for the $^3F_4$ manifold is sensitive to small changes in the B_{nm} as a result of the relatively large matrix elements having terms that change sign with respect to each other. Using the lattice-sum B_{nm} to predict the splitting of $^3F_4$, we find relatively large disagreement between the calculated and observed Stark levels 5558 and 5624 cm^{-1}. We can improve agreement between the calculated Stark levels and the experimental Stark levels reported in Table IV, column 2, by a least-squares fitting analysis that varies the B_{nm} and centroid parameters. The rms obtained from this calculation is 10 cm^{-1} for 37 calculated-to-observed levels, and the final set of B_{nm} are listed in column 4 of Table III. The calculated splitting with this set of parameters is given in column 4 of Table IV. The symmetry labels Γ_1 or Γ_2 (each nondegenerate), and Γ_3 (twofold degenerate) are listed in column 5 of Table IV and represent the predicted labels using the lattice-sum B_{nm} parameters for the calculated splitting given in column 3. We found no reordering of these labels between the two calculations although considerable improvement for the numerical splitting within the $^3F_4$ and $^3H_4$ manifolds is obtained using the least-squares B_{nm} values as given in column 4 of Table III.

Efforts to establish the energy of the $^3P_0$ of Tm^{3+} in AlN experimentally have been elusive. The hosts we have used as guides predict $^3P_0$ at 35 604 cm^{-1}, [LaF_3 (Ref. 34)], 35 372 cm^{-1} [$Y_3Al_5O_{12}$ (Ref. 33)], and 35 346 cm^{-1} [Y_2O_3 (Ref. 35)]. Based on intensity calculations, we predict that that largest transition probabilities from $^3P_0$ to lower-energy multiplets would be to $^3F_2$, which depends only on U_2, $^3F_4$, which depends only on U_4, and possibly $^3H_6$ which depends on U_6. The form of the dipole operators, U_n, and the values of the matrix elements are given by Kaminskii[43] and are based on earlier work by Judd.[44] We have not found a pattern of the splitting of $^3F_4$ and $^3H_6$ we can associate with any reasonable emitting level for $^3P_0$. We do find an isolated group of emission lines at 513.76, 514.38, and 516.66 nm that would place the $^3P_0$ relative to our current assignment for $^3F_2$ (based on $^1I_6 \rightarrow {}^3F_2$ in Table I) around 34 800 cm^{-1} which is lower than our predicted value around 35 200 cm^{-1}. Moreover, the observed energy separation between these three transitions given a $^3F_2$ splitting of 24 and 85 cm^{-1} compared with the energy separation based on the predicted splitting in Table IV (column 3) of 76 and 43 cm^{-1}, respectively. This experimental data is insufficient for us to reconsider our least-squares fitting analysis with this set representing the splitting of $^3F_2$. To accommodate the ordering of this experimental splitting for $^3F_2$ requires a change in sign of at least one of the second or fourth order B_{nm} terms. We prefer to stay with results obtained using the lattice-sum derived B_{nm} splitting predicted in Table IV, column 3.

V. SUMMARY OF RESULTS

In summary, we present a crystal-field splitting analysis of the energy levels of Tm^{3+} implanted in AlN based on the splitting of individual $^{2S+1}L_J$ multiplet manifolds of the ground-state electronic configuration $4f^{12}$ by a crystalline electric field whose parameters B_{nm} are determined from a lattice-sum calculation that assumes the Tm^{3+} ions replace the Al^{3+} ions in C_{3v} sites in the AlN lattice. Emitting Stark levels from the $^1I_6$, $^1D_2$, and $^1G_4$ manifolds establish the splitting of the $^3H_6$, $^3F_4$, $^3H_5$, $^3H_4$, $^3F_3$, $^3F_2$, and $^1G_4$ manifolds through an energy-difference analysis of more than 100 observed transitions between 290 and 820 nm. Two separate groupings of transitions we identify as $^3P_1 \rightarrow {}^3H_5$ and $^3P_1 \rightarrow {}^3F_3$ assist in establishing the energy and the splitting of the $^3P_1$ manifold. Additional emission is observed which may involve both electronic and vibronic sidebands, but are not identified due to their complexity. Vibronic sidebands corresponding to local phonon modes have been more clearly observed recently in Gd^{3+} doped AlN.[10] Emission from $^3P_2$ and $^3P_0$ is possible, but we lack direct evidence for the energy of the emitting Stark level. Without this information we cannot quantify the nephelauxetic effect[45] (the shift of the centroids in AlN relative to LaF_3, $Y_3Al_5O_{12}$, and Y_2O_3 hosts for Tm^{3+}) through our present analysis. The origin of the nephelauxetic effect,[45] whether due to changes in covalency or polarizabilities of host lattice constituents, is worth further study. Future modeling of the crystal-field splitting will be designed to include covalent contributions neglected in the present calculations.

In our analyses of the CL spectra of Gd^{3+} and Tm^{3+} in AlN,[11,12] we pointed out in some detail the conditions under which the samples were prepared. Following different steps, such as using different annealing temperatures, substrates, or methods of doping, we can bring about different microscopic environments for Tm^{3+} in the lattice. The details of the manifold spectra will change due to changes in local symmetry at the Tm^{3+} ion site and the crystal-field splitting of the levels will be different. Unfortunately, we cannot make such a comparative analysis for the CL spectra of Tm^{3+} in AlN samples in which the thulium is added during sample growth since the reports given in the literature[46,47] do not show a specific crystal-field splitting,[46] or values for the splitting are not reported.[47]

An interesting and potentially important question arises from the collective work of investigators in Refs. 46 and 47, and our own work, namely, will different approaches to materials processing lead to improved efficiency in optoelectronic devices that employ these materials as components? From what spectroscopic information that is available in the literature, and from our continuing modeling studies on these data,[29–31] we find that by altering the preparation and annealing conditions one can affect different ligand arrangements and different embedding configurations of these complexes in the host matrices.[11] The results can appear as an enhancement to individual transition line strengths, excitation cross sections, and relative changes in branching ratios for emitting rare earth ions.[11,12] This particularly affects Yb^{3+}, Tm^{3+}, Eu^{3+}, and Pr^{3+}, in GaN and AlN. Some of these details we have reported earlier by recognizing changes also promoted by the nephelauxetic effect.[29–31] While more work needs to be done in detailed analyses of the spectroscopic data, similar to the study reported here, it is clear that a wide field remains open for future investigations on the path to highly efficient lanthanide-doped wide band-gap semiconductors for use in optoelectronic devices.

[1] J.D. MacKenzi, C.B. Abernathy, S.J. Pearton, U. Hömmerich, X. Wu, R.N. Schwartz, R.G. Wilson, and J.M. Zavada, Appl. Phys. Lett. **69**, 2083 (1996).
[2] S.J. Pearson, C.R. Abernathy, J.D. MacKenzie, U. Hömmerich, X. Wu, R.G. Wilson, R.N. Schwartz, J.M. Zavada, and F. Ren, Appl. Phys. Lett. **71**, 1807 (1997).
[3] S.J. Pearson, C. Abernathy, J.D. MacKenzie, U. Hömmerich, J.M. Zavada, R.G. Wilson, and R.N. Schwartz, J. Vac. Sci. Technol. A **16**, 1627 (1998).
[4] X. Wu, U. Hömmerich, J. MacKenzie, C. Abernathy, S. Pearton, R. Wilson, R. Schwartz, and J. Zavada, J. Lumin. **72–74**, 284 (1997).
[5] K. Gurumurugan, H. Chen, G.R. Harp,W.M. Jadwisienczak, and H.J. Lozykowski, Appl. Phys. Lett. **74**, 3008 (1999).
[6] W.M. Jadwisienczak, H.J. Lozykowski, F. Perjeru, H. Chen, M. Kordesch, and I.G. Brown, Appl. Phys. Lett. **76**, 3376 (2000).
[7] V.I. Dimitrova, P.G. Van Patten, H.H. Richardson, and M.E. Kordesch, Appl. Phys. Lett. **77**, 478 (2000).
[8] *Properties of Advanced Semiconductor Materials, GaN, AlN, InN, BN, SiC, SiGe*, edited by M. Levinshtein, S. Rumyantsev, and M. Shur (Wiley, New York, 2001).
[9] H.J. Lozykowski, W.M. Jadwisienczak, and I.G. Brown, Appl. Phys. Lett. **76**, 861 (2000).
[10] U. Vetter, J. Zenneck, and H. Hofsäss, Appl. Phys. Lett. **83**, 2145 (2004).
[11] U. Vetter, J.B. Gruber, B. Zandi, M.F. Reid, and H. Hofsäss, Fourth International Spring Workshop on Spectroscopy, Structure and Synthesis of Rare Earth Systems, Presentation 023, Ladek Zdrój, Poland, June 21–26, 2003 (unpublished).
[12] J.B. Gruber, U. Vetter, H. Hofsäss, B. Zandi, and M. Reid, Phys. Rev. B **69**, 195202 (2004).
[13] J.T. Torvik, C.H. Qiu, R.J. Feuerstein, J.I. Pankove, and F. Namavar, J. Appl. Phys. **81**, 6343 (1997).
[14] J.T. Torvik, R.J. Feuerstein, C.H. Qiu, J.I. Pankove, and F. Namavar, J. Appl. Phys. **82**, 1824 (1997).
[15] D.M. Hansen, R. Zhang, N.R. Perkins, S. Safvi, L. Zhang, K.L. Bray, and T.F. Kuech, Appl. Phys. Lett. **72**, 1244 (1998).
[16] A.J. Steckl, M. Garter, R. Birkhan, and J. Scofield, Appl. Phys. Lett. **73**, 2450 (1998).
[17] H. Heikenfeld, M. Garter, D. Lee, R. Birkhahn, and A. Steckl, Appl. Phys. Lett. **75**, 1189 (1999).
[18] H.J. Lozykowski, W.M. Jadwisienczak, and I.G. Brown, Solid State Commun. **110**, 253 (1999).
[19] H.J. Lozykowski, W.M. Jadwisienczak, and I.G. Brown, J. Appl. Phys. **88**, 210 (2000).
[20] L. van Pieterson, M.F. Reid, R.T. Wegh, S. Soverna, and A. Meijerink, Phys. Rev. B **65**, 045113 (2002).
[21] C. Ronda, T. Jüstel, and H. Nikol, J. Alloys Compd. **275–277**, 669 (1998).
[22] J. Yum, S. Seo, S. Lee, and Y. Sung, J. Electrochem. Soc. **150**, H47 (2003).
[23] W.M. Jadwisienczak, H.J. Lozykowski, I. Berishev, A. Bensaoula, and I. Brown, J. Appl. Phys. **89**, 4384 (2001).
[24] U. Vetter, M.F. Reid, H. Hofsäss, C. Ronning, J. Zenneck, M. Dietrich, and the ISOLDE Collaboration, Mater. Res. Soc. Symp. Proc. **743**, L6.16 (2003).
[25] U. Hömmerich, E.E. Nyein, D.S. Lee, A.J. Steckl, and J.M. Zavada, Appl. Phys. Lett. **83**, 4556 (2003).
[26] U. Wahl, A. Vantomme, G. Langouche, J.P. Araújo, L. Peralta, J.G. Correia, and the ISOLDE Collaboration, J. Appl. Phys. **88**, 1319 (2000).
[27] U. Wahl, A. Vantomme, J. DeWachter, R. Moons, G. Langouche, J.G. Marques, J.G. Correia, and the ISOLDE Collaboration, Phys. Rev. Lett. **79**, 2069 (1997).
[28] U. Wahl, A. Vantomme, G. Langouche, and J.P. Araújo, Nucl. Instrum. Methods Phys. Res. B **175–177**, 262 (2001).
[29] J.B. Gruber, B. Zandi, H.J. Lozykowski, W.M. Jadwisienczak, and I.G. Brown, J. Appl. Phys. **89**, 7973 (2001).
[30] J.B. Gruber, B. Zandi, H.J. Lozykowski, and W.M. Jadwisienczak, J. Appl. Phys. **91**, 2929 (2002).
[31] J.B. Gruber, B. Zandi, H.J. Lozykowski, and W.M. Jadwisienczak, J. Appl. Phys. **92**, 5127 (2002).
[32] W.T. Carnall, P.R. Fields, and K. Rajnak, J. Chem. Phys. **49**, 4412 (1968); **49**, 4424 (1968); **49**, 4443 (1968); **49**, 4447 (1968); **49**, 4450 (1968).
[33] J.B. Gruber, M.E. Hills, R.M. Macfarlane, C.A. Morrison, G.A. Turner, G.J. Quarles, G.J. Kintz, and L. Esterowitz, Phys. Rev. B **40**, 9464 (1989).
[34] W.T. Carnall, P.R. Fields, J. Morrison, and R. Sarup, J. Chem. Phys. **52**, 4054 (1970).
[35] R.P. Leavitt, J.B. Gruber, N.C. Chang, and C.A. Morrison, J. Chem. Phys. **76**, 4775 (1982).
[36] H.J. Lozykowski, Phys. Rev. B **48**, 17 758 (1993), and references therein.
[37] C.A. Morrison and R.P. Leavitt, "*Programs at HDL for Calculating Optical Properties of Rare Earth Ions in Single Crystal Hosts*," Harry Diamond Laboratories, Adelphi, MD, October 6, 1992 (unpublished report).
[38] C.A. Morrison, R.P. Leavitt, and D.E. Wortman, J. Chem. Phys. **73**, 2580 (1980).
[39] C.A. Morrison, *Angular Momentum Theory Applied to Interactions in Solids* (Springer, New York, 1980).
[40] C.A. Morrison and R.P. Leavitt, in *Handbook on the Physics and Chemistry of Rare Earths*, edited by K.A. Gschneidner and L. Eyring (North-Holland, New York, 1982), pp. 461–692.
[41] R. Wyckoff, *Crystal Structures, Vol. 3* (Interscience, New York, 1965).
[42] *International Tables for x-Ray Crystallography, Vol. 1*, edited by N. Henry and K. Lonsdale (Kynoch, 1969).
[43] A.A. Kaminskii, *Laser Crystals* (Springer, Berlin, 1981).
[44] B.R. Judd, *Operator Techniques in Atomic Spectroscopy* (McGraw-Hill, New York, 1963).
[45] R. Reisfeld and C.K. Jørgensen, *Lasers and Excited States of Rare Earths* (Springer, New York, 1977).
[46] D.S. Lee and A.J. Steckl, Appl. Phys. Lett. **81**, 2094 (2003).
[47] U. Hömmerich, E.E. Nyein, D.S. Lee, A.J. Steckl, and J.M. Zavada, Appl. Phys. Lett. **83**, 4556 (2003).